Journal of Quantitative Spectroscopy & Radiative Transfer 300 (2023) 108528

Contents lists available at ScienceDirect

Journal of Quantitative Spectroscopy & Radiative Transfer

journal homepage: www.elsevier.com/locate/jqsrt

Realization of the nonreciprocal thermal radiation by the front and back sides of the Weyl semimetal-dielectric multilayer structures

You-Ming Liu[a], Yuan-Kun Shi[a], Dan Zhang[b], Hai-Feng Zhang[a,*]

[a] College of Electronic and Optical Engineering & College of Flexible Electronics (Future Technology), Nanjing University of Posts and Telecommunications, Nanjing, 210023, China
[b] College of Information Science and Technology, Nanjing Forestry University, Nanjing, 210037, China

ARTICLE INFO

Article history:
Received 15 October 2022
Revised 31 January 2023
Accepted 9 February 2023
Available online 14 February 2023

Keywords:
Kirchhoff's law
Multilayer structures
Weyl semimetal
Nonreciprocal thermal radiation
Transfer matrix method

ABSTRACT

This work proposes the Weyl semimetal-dielectric multilayer structures (WDMSes), both sides of which can realize nonreciprocal thermal radiation. Utilizing the transfer matrix method, the absorptivity α_q and emissivity e_q are calculated in the mid-infrared wave range. The absorption can be attributed to the defect modes. For both sides of the WDMSes, it is found the nonreciprocity originates as the incident angle is around 15° and a wider incident angle tends to enhance it. By increasing the angle to 45°, the stronger nonreciprocal thermal radiation for the front side is revealed at the wavelength of 4.692 μm and 3.890 μm. In the same way, for the back side, it is displayed at the wavelength of 4.692 μm and 3.896 μm. The relevant factors including the temperature of the Weyl semimetal, the thickness of the dielectric layer unit, the thickness of the defect layer, and the period of the structure are discussed. They can affect the nonreciprocity, as well as shift the absorption and emission bands in the wave and angular range. This work can be applied to heat radiation transfer media, energy conversion devices, thermal storage and emitter, and so on.

1. Introduction

Thermal radiation is such a process that objects with a temperature over 0 K transmit energy outwards by electromagnetic (EM) waves [1,2]. It mainly relies on visible and infrared wavelengths. Based on the traditional Kirchhoff's law, the objects in the thermal equilibrium always follow the pattern, that the directional spectral emissivity is equal to the absorptivity on the surface. Yet, the balance in some way blocks the improvement of the applied energy conversion [3,4]. In recent years, many works have been done seeking to break it and magneto-optical materials play a significant role. In essence, it can be attributed to the magneto-optical materials' breaking the time-reversal symmetry [5,6]. By these materials, the directional spectral emissivity doesn't equate with the absorptivity on the surface numerally. This is so-called nonreciprocity. Zhu et al. [7] proposed a grating structure with the introduction of the InAs to realize the nonreciprocal radiation. Zhao et al. [8] placed the dielectric gratings on the InAs layers to bring in the nonreciprocal thermal radiation while the required external magnetic field is only 0.3 T at a low level. Apart from the magneto-optical materials, the Weyl semimetals with strong nonreciprocity yet independent of the external magnetic fields draw widespread interest as well [9–13].

In terms of structure, topological insulators [14], gratings [7,8,15,16], prisms [12], and multilayer structures (MSes) [9,11,17,18] are widely made use of to achieve nonreciprocity. Particularly, the MSes, which are composed of stacked layers take advantage of the simplicity of the constitution and fabrication. The MSes with the introduction of nonreciprocal materials can demonstrate kinds of optical properties, including unidirectional propagation [19–21], Faraday rotation [22,23], Goos-Hänchen shift [24,25], photonic band gaps [26–28], and so on. What's more, the methods to achieve strong absorption are relatively comprehensive. The introduction of the metal layers leads to absorption, due to the high lossy property [29,30]. Defect modes in the MSes localized fields in the lossy cavity resulting in the absorption [31]. The optical Tamm state is also an ideal way [32]. Based on these means, Wu et al. [17] violated Kirchhoff's law at an incident angle θ=30°. Wu et al. [18] combined the Tamm state with the magneto-optical layers to break the balance between absorption and emission at a wavelength shorter than 16 μm with an incident angle θ=60°.

Generally speaking, in the former works, the nonreciprocal property of the MSes is operated in the long wave infrared range and large incident angles. Continuously narrowing the incident angle and wavelength still needs effort. For one thing, higher-temperature objects tend to radiate more heat energy over shorter

* Corresponding author.
E-mail addresses: hanlor@163.com, hanlor@njupt.edu.cn (H.-F. Zhang).

https://doi.org/10.1016/j.jqsrt.2023.108528
0022-4073/

wavelength bands. For another thing, reducing the angle, required to violate the conventional Kirchhoff's law, will enable the thermal devices to operate over a wider range of the orientation angle. In addition, the properties of thermal radiation devices are temperature-dependent, but few focuses have been placed on them in the previous works. Moreover, it makes sense to take into account the properties of emitting and absorbing the heat by both the front side (FS) and the back side (BS) of the multilayer structures. For the EM wave at a specific wavelength and directional angle, if one side of a multilayer reveals strong absorption, while the other side can strongly emit it, it will enable the multilayers to have the dual function-heat storage or emitter. Also, considering the properties of both sides can help apply the multilayers to the heat transfer media and double-sided heat sink media.

This work proposes the Weyl semimetal-dielectric multilayer structures (WDMSes) to realize the nonreciprocal thermal radiation in the mid-infrared wave range. The absorption and emission can be attributed to the defect layers. Here, the nonreciprocal thermal properties of the FS and BS of the structure are taken into consideration. η_q is borrowed to describe nonreciprocity. For both the FS and BS, the WDMSe is optimized to achieve η_q>0.9 at a smaller angle of around 15°. The nonreciprocity is also discussed with the temperature ranging from 200 K to 400 K. Besides, relevant parameters including incident angle, thicknesses of the dielectric layer unit, defect thickness, and periods of the structure are adjusted to investigate the influences. The numeral simulations are based on the transfer matrix method (TMM) [33] This work can offer references for designing heat transfer media, energy conversion devices, thermal storage and emitter, and so on.

2. Model and theoretical method

Figure 1 displays the schematic of the WDMSes, consisting of the two general dielectric layers (H and L) and the Weyl semimetal defects (W). Here, the layers are placed stratified along the *z*-direction, and for simplicity, the whole structure can be described in the form of (HL)W(HL)^{N}W(HL), where N denotes the period value. The two general dielectric layers H and L can be taken as a unit represented as U. Then the structure can also be displayed as UWU^{N}WU. The EM waves propagate parallel to the *xoz* plane and couple into the WDMSes with an incident angle θ on the surface. The multilayer structures possess both the front and back sides. In this paper, the side where the H layer meets the free space is referred to as the FS, while the side where the L layer meets the free space is the BS. Because of the anisotropic permittivity of the W layers, only the transverse magnetic (TM) waves are discussed in this work, of which the magnetic fields are polarized positively along the *y*-axis. The layers H and L are the synthetic dielectrics, the refractive indices for which are signified as n_H=4.1 and n_L=1.2. To get better nonreciprocal thermal radiation, the thicknesses of the H and L layers are optimized as d_H= 0.2439 μm and d_L=1.25 μm. In the same way, the thickness of the W layer is set as d_W= 1 μm.

As denoted before, the relative permittivity of the W represents the form of anisotropy [34]:

$$\boldsymbol{\varepsilon}_{\mathbf{r}} = \begin{pmatrix} \varepsilon_d & 0 & j\varepsilon_a \\ 0 & \varepsilon_d & 0 \\ -j\varepsilon_a & 0 & \varepsilon_d \end{pmatrix}, \tag{1}$$

where the functions of ε_d and ε_a are expressed as [34]:

$$\varepsilon_a = \frac{be^2}{2\pi^2\hbar\omega\varepsilon_0} \tag{2}$$

$$\varepsilon_d = \varepsilon_b + i\frac{r_s g}{6\mathrm{Re}(\Omega)}\Omega G\left(\frac{E_F\Omega}{2}\right) - \frac{r_s g}{6\pi\,\mathrm{Re}(\Omega)}\left\{\frac{4}{\Omega}\left[1+\frac{\pi^2}{3}\left(\frac{k_BT}{E_F}\right)^2\right] + 8\Omega\int_0^{\xi_c}\frac{G(E_F\xi)-G\left(\frac{E_F\Omega}{2}\right)}{\Omega^2-4\xi^2}\xi d\xi\right\} \tag{3}$$

Here, ε_b is the background permittivity, E_F and E_c are the chemical potential and the cutoff energy, beyond which the band dispersion is no longer linear. The relation between the two meets the equation E_c=$\xi_c E_F$. E_F is related to the temperature T [34]:

$$E_F = \frac{2^{1/3}[9E_F(0)^3+\sqrt{81E_F(0)^6+12\pi^6k_B^6T^6}]^{2/3} - 2\pi^2 3^{1/3}k_B^2T^2}{6^{2/3}[9E_F(0)^3+\sqrt{81E_F(0)^6+12\pi^6k_B^6T^6}]^{1/3}} \tag{4}$$

The normalized complex frequency is written as Ω= $\hbar(\omega+j\tau^{-1})/E_F$, where τ^{-1} is the Drude damping rate. $G(E) = n(-E) - n(E)$ and $n(E)$ is the Fermi distribution function. The effective fine-structure constant r_s is equal to $e_0^2/(4\pi\varepsilon_0\hbar v_F)$, where v_F is the Fermi velocity. In addition, g is the number of Weyl points. The values of these parameters are taken as ε_b=6.2, ξ_c=3, τ=1000 fs, g = 2, b = 8.5 × 10^8 m^{-1}, v_F=0.85 × 10^5 m/s and E_F=0.30 eV at T = 300 K [34].

Supposing T = 300 K, the parameter γ=$|\varepsilon_a|/|\varepsilon_d|$ is borrowed to weigh the nonreciprocal properties of the Weyl semimetals [17].

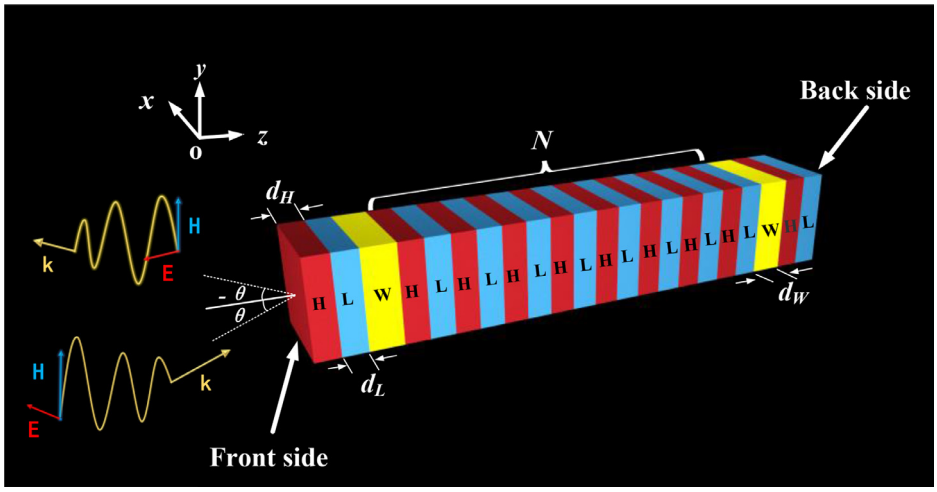

Fig. 1. The schematic of the given WDMSes.

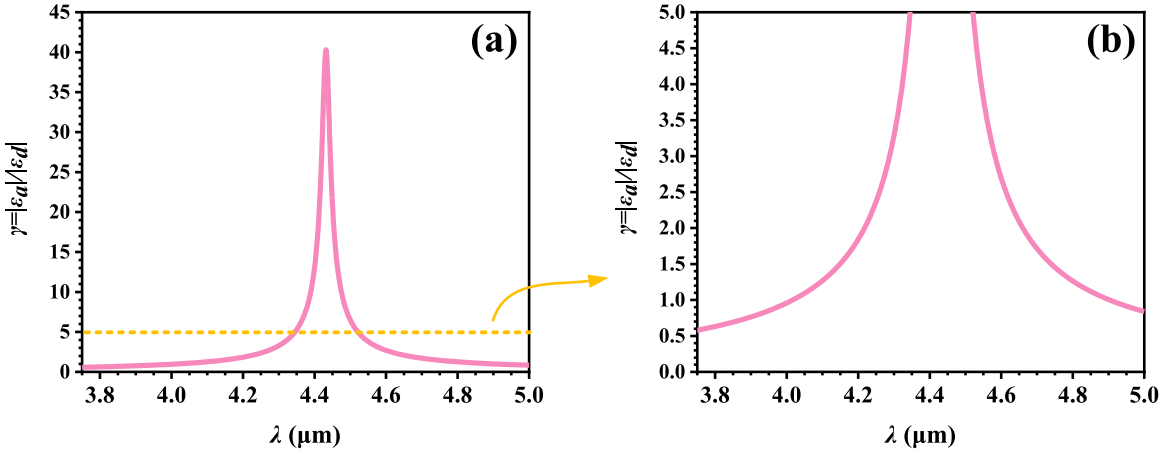

Fig. 2. (a) the curve of $\gamma=|\varepsilon_a|/|\varepsilon_d|$ related to the wavelength in the case of $T = 300$ K and (b) local enlarged view of (a) where the range of γ is from 0 to 5.

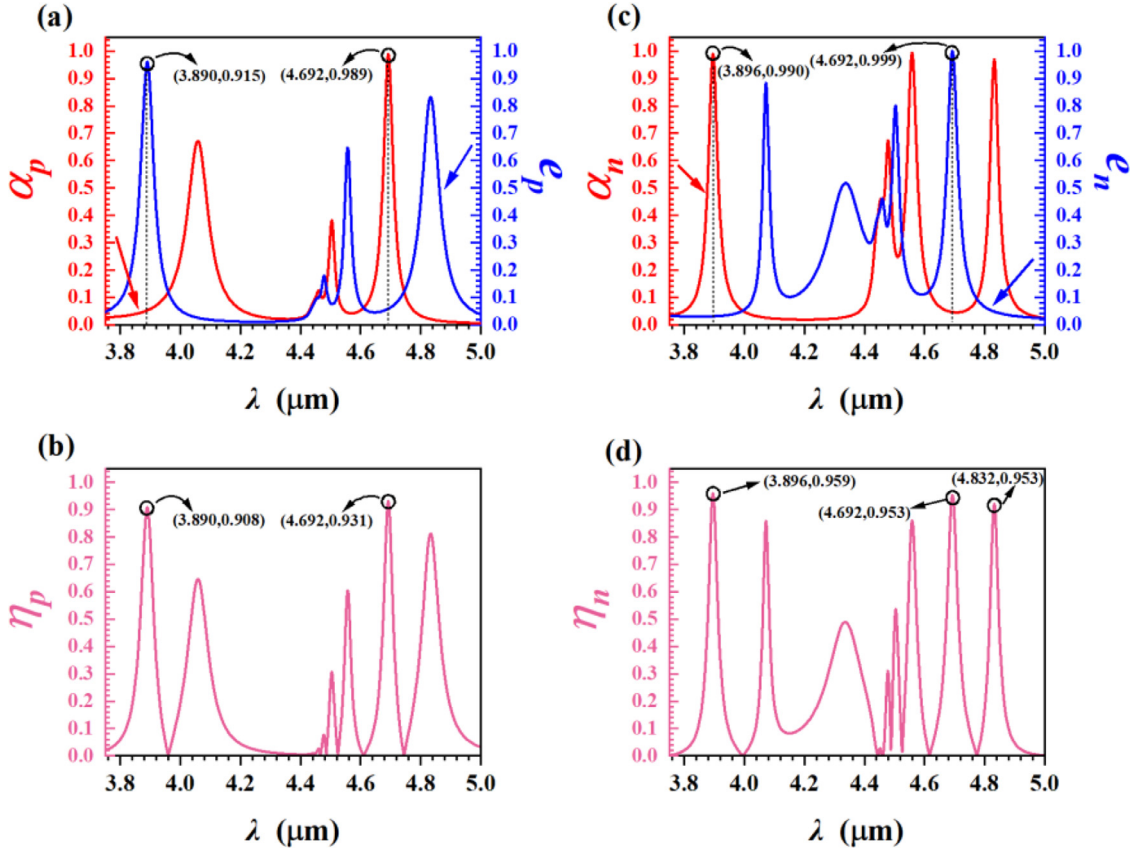

Fig. 3. The spectra of α_q, e_q and η_q for the FS and BS relating to λ. (a) α_p and e_p for the FS, (b) η_p for the FS, (c) α_n and e_n for the BS, and (d) η_n for the BS.

Figs.2(a) and (b) give the curves of γ in the studied wavelength domain. Clearly, with the rising wavelength, γ increases then decreases. In Fig. 2(a), γ reaches its maximum at λ=4.432 μm and it is 40.297. As shown in the local enlargement in Fig. 2(b), the minimum of γ is 0.580 at λ=3.75 μm. In the range from 4.345 μm to 4.521 μm. γ exceeds 5 completely. From the value of γ, the property of the Weyl semimetals is superior to that of the nonreciprocal materials used in Refs. [17] and [35].

For the TM waves, the effective refractive index for the TM wave is written as:

$$n_W = \sqrt{(\varepsilon_d^2 - \varepsilon_a^2)/\varepsilon_d} \tag{5}$$

The transfer matrix of the W layers under the TM waves can be derived as [33]:

$$\mathbf{M}_W = \begin{pmatrix} \cos(k_{Wz}d_W) + \frac{k_{Wx}\varepsilon_a}{k_{Wz}\varepsilon_d}\sin(k_{Wz}d_W) & -\frac{j}{\eta_W}[1+(\frac{k_{Wx}\varepsilon_a}{k_{Wz}\varepsilon_d})^2]\sin(k_{Wz}d_W) \\ -j\eta_W \sin(k_{Wz}d_W) & \cos(k_{Wz}d_W) - \frac{k_{Wx}\varepsilon_a}{k_{Wz}\varepsilon_d}\sin(k_{Wz}d_W) \end{pmatrix} \tag{6}$$

Here, $\eta_W = \sqrt{\varepsilon_0/\mu_0}n_W/\cos(\theta_W)$, where θ_w denotes the incident angles on the W layers, and the wave vector in the *xoz* plane is decomposed to each direction $k_{Wx}=(2\pi/\lambda)\cdot n_W\cdot\sin\theta_W$ and $k_{Wz}=(2\pi/\lambda)\cdot n_W\cdot\cos\theta_W$, where λ is the wavelength of the TM waves in the free space.

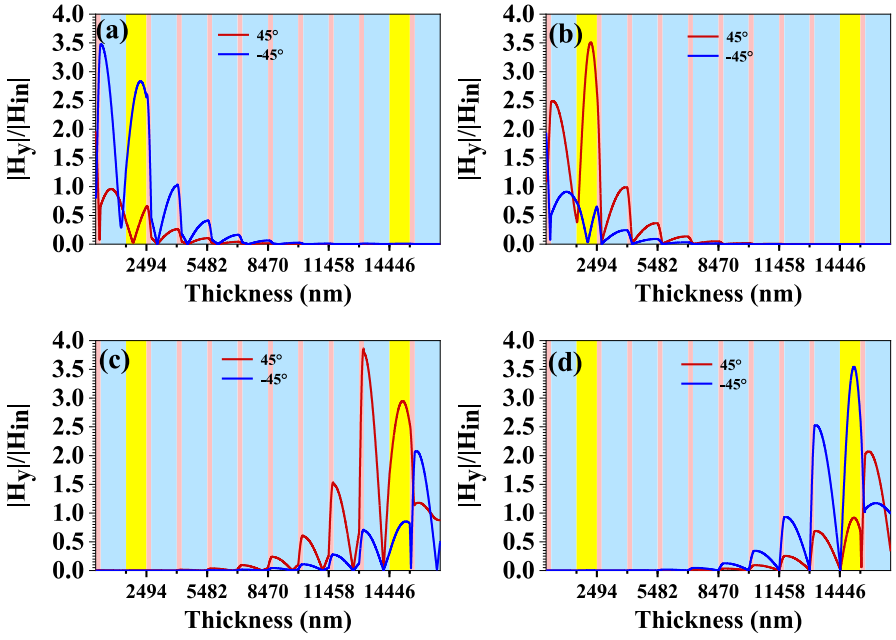

Fig. 4. The distribution of magnetic fields along the stratified layers for the FS and BS. (a) λ=3.890 μm for the FS, (b) λ=4.692 μm for the FS, (c) λ=3.896 μm for the BS, and (d) λ=4.692 μm for the BS.

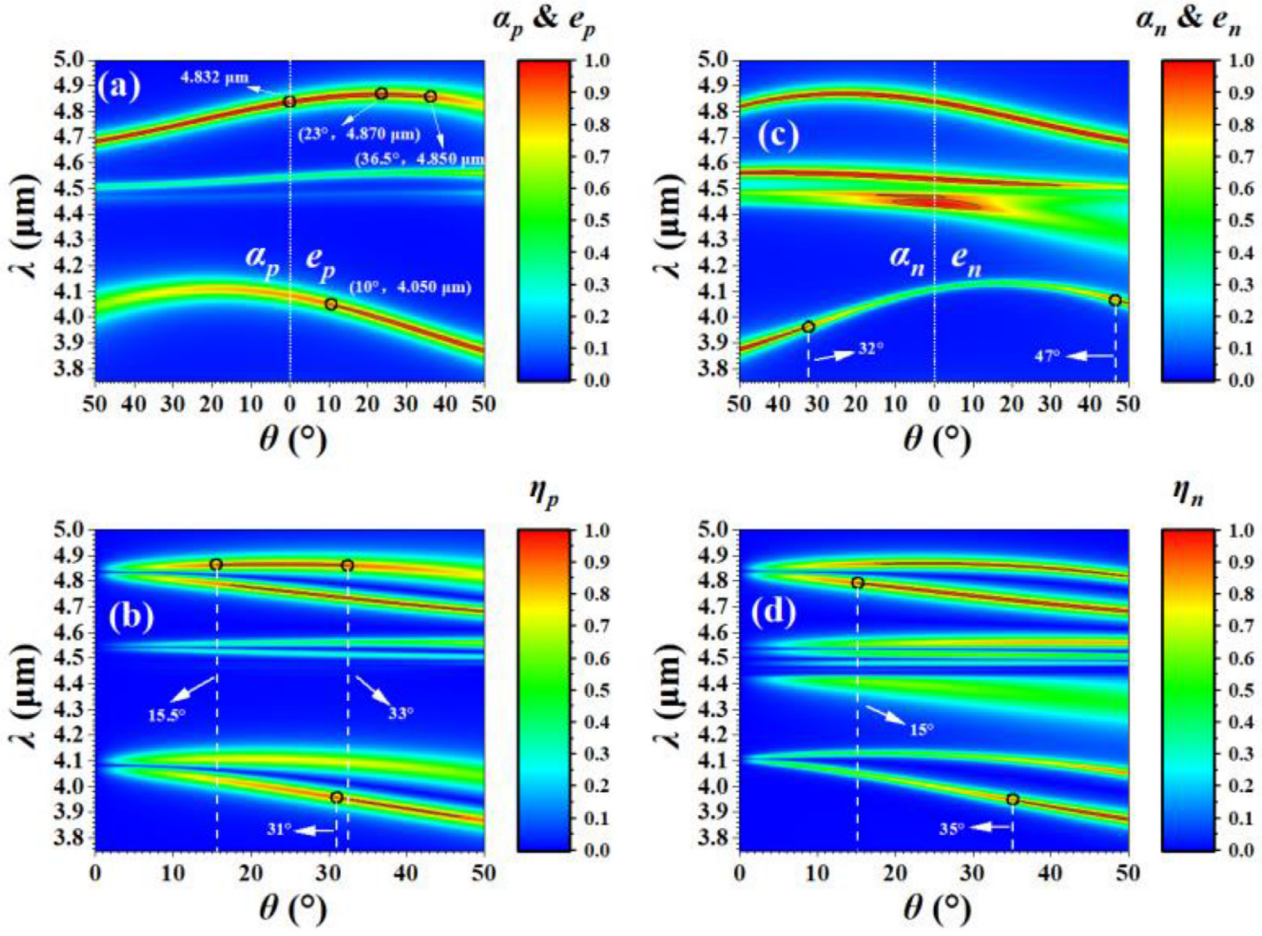

Fig. 5. The contour maps of α_q, e_q and η_q for the FS and the BS. (a) α_p and e_p for the FS, (b) η_p for the FS, (c) α_n and e_n for the BS, and (d) η_n for the BS.

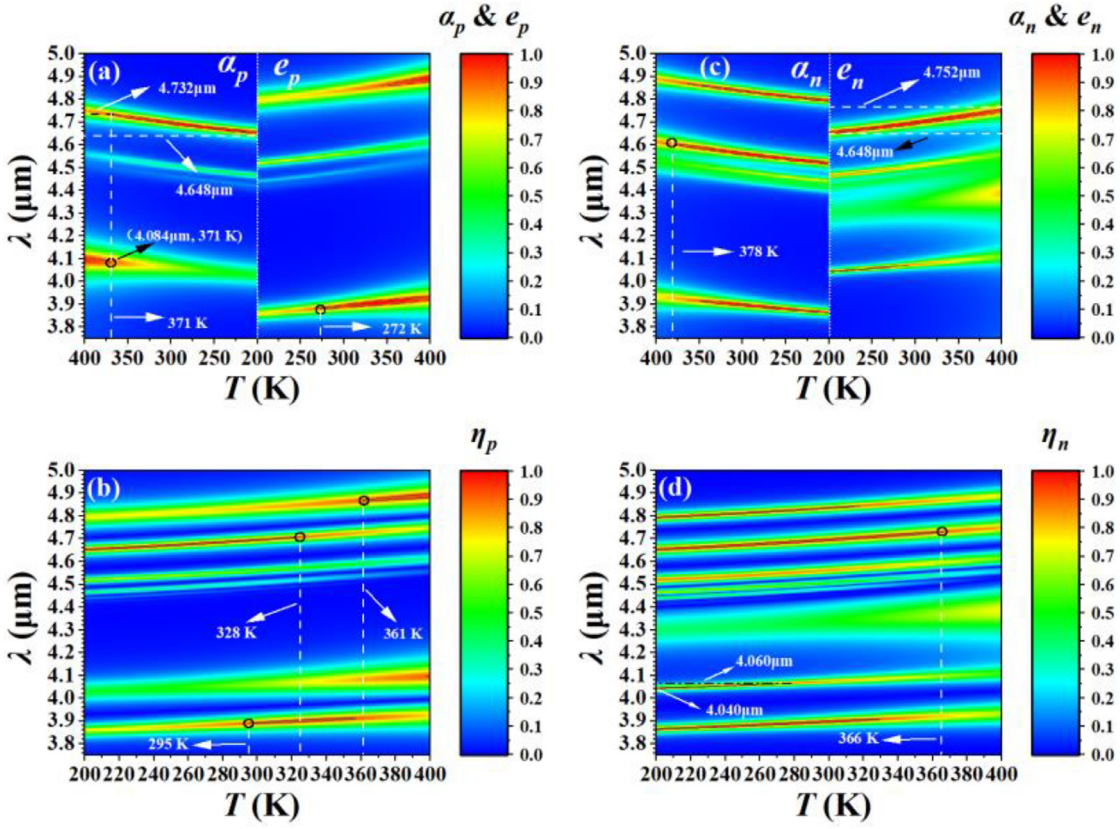

Fig. 6. Simulated performance of α_q, e_q and η_q for the FS and BS under different T. (a) α_p and e_p for the FS, (b) η_p for the FS, (c) α_n and e_n for the BS, and (d) η_n for the BS.

The matrix for the dielectric layer H or L is deduced as [36]:

$$\mathbf{M}_i = \begin{pmatrix} \cos(k_{iz}d_i) & -\frac{j}{\eta_i}\sin(k_{iz}d_i) \\ -j\eta_i \sin(k_{iz}d_i) & \cos(k_{iz}d_i) \end{pmatrix} \tag{7}$$

where i = H, L. k_{iz}=$(2\pi/\lambda)\cdot n_i \cdot \sin\theta_i$ is the z component of the incident wave vector. In the same way, $\eta_i = \sqrt{\varepsilon_0/\mu_0}n_i/\cos(\theta_i)$ and θ_i represents the incident angles on the surface of the i layers.

Through the proposed WDMSes, the input and output EM fields can be joined by the total transfer matrix of the structure:

$$\begin{pmatrix} E_1 \\ H_1 \end{pmatrix} = \begin{pmatrix} M_{11} & M_{12} \\ M_{21} & M_{22} \end{pmatrix} \begin{pmatrix} E_{N+1} \\ H_{N+1} \end{pmatrix} = \mathbf{M} \begin{pmatrix} E_{N+1} \\ H_{N+1} \end{pmatrix}. \tag{8}$$

For the EM waves coupling into the structure from the front side, the **M** can be written as:

$$\mathbf{M_{positive}} = (\mathbf{M}_H\mathbf{M}_L) \times \mathbf{M}_W \times (\mathbf{M}_H\mathbf{M}_L)^N \times \mathbf{M}_W \times (\mathbf{M}_H\mathbf{M}_L), \tag{9}$$

$$\mathbf{M_{positive}} = \begin{pmatrix} M_p^{11} & M_p^{12} \\ M_p^{21} & M_p^{22} \end{pmatrix}. \tag{10}$$

For the ones from the back side, the **M** is given by:

$$\mathbf{M_{negative}} = (\mathbf{M}_L\mathbf{M}_H) \times \mathbf{M}_W \times (\mathbf{M}_L\mathbf{M}_H)^N \times \mathbf{M}_W \times (\mathbf{M}_L\mathbf{M}_H), \tag{11}$$

$$\mathbf{M_{negative}} = \begin{pmatrix} M_n^{11} & M_n^{12} \\ M_n^{21} & M_n^{22} \end{pmatrix}. \tag{12}$$

One can obtain the reflection coefficient r_p and transmission coefficient t_p for the waves from the front side, as well as the reflection coefficient r_n and transmission coefficient t_n for the waves from the back side, with an incident angle θ [33]:

$$r_p(\theta) = -\frac{M_p^{11}\eta_0 + M_p^{12}\eta_0\eta_{N+1} - M_p^{21} - M_p^{22}\eta_{N+1}}{M_p^{11}\eta_0 + M_p^{12}\eta_0\eta_{N+1} + M_p^{21} + M_p^{22}\eta_{N+1}} \tag{13}$$

$$t_p(\theta) = \frac{2\eta_0}{M_p^{11}\eta_0 + M_p^{12}\eta_0\eta_{N+1} + M_p^{21} + M_p^{22}\eta_{N+1}} \tag{14}$$

$$r_n(\theta) = -\frac{M_n^{11}\eta_0 + M_n^{12}\eta_0\eta_{N+1} - M_n^{21} - M_n^{22}\eta_{N+1}}{M_n^{11}\eta_0 + M_n^{12}\eta_0\eta_{N+1} + M_n^{21} + M_n^{22}\eta_{N+1}} \tag{15}$$

$$t_n(\theta) = \frac{2\eta_0}{M_n^{11}\eta_0 + M_n^{12}\eta_0\eta_{N+1} + M_n^{21} + M_n^{22}\eta_{N+1}} \tag{16}$$

For the WDMSes are lain in the free space, η_0 and η_{N+1} are equal to η_{air}. In the case of the TM waves, $\eta_{air} = \sqrt{\varepsilon_0/\mu_0}n_{air}/\cos(\theta_{air})$. Thus, the related reflectivity $R_q(\theta)$ and transmissivity $Tr_q(\theta)$ can be expressed as [1,33]:

$$R_q(\theta) = |r_q(\theta)|^2, \tag{17}$$

$$Tr_q(\theta) = |t_q(\theta)|^2, \tag{18}$$

where q = p,n.

Assuming the weak transmissivity through the structure, the formula of the absorptivity and emissivity for the FS or BS is given:

$$\alpha_q(\theta) = 1 - R_q(\theta), \tag{19}$$

$$e_q(\theta) = 1 - R_q(-\theta). \tag{20}$$

The detailed derivation of the absorptivity and emissivity is given in Appendix B based on energy conservation. In Appendix B, it is also verified the EM waves transmitted through the structure in this paper are weak, whatever the incident angles or wavelengths are. As a result, there also exists one relationship that:

$$\alpha_q(-\theta) = 1 - R_q(-\theta). \tag{21}$$

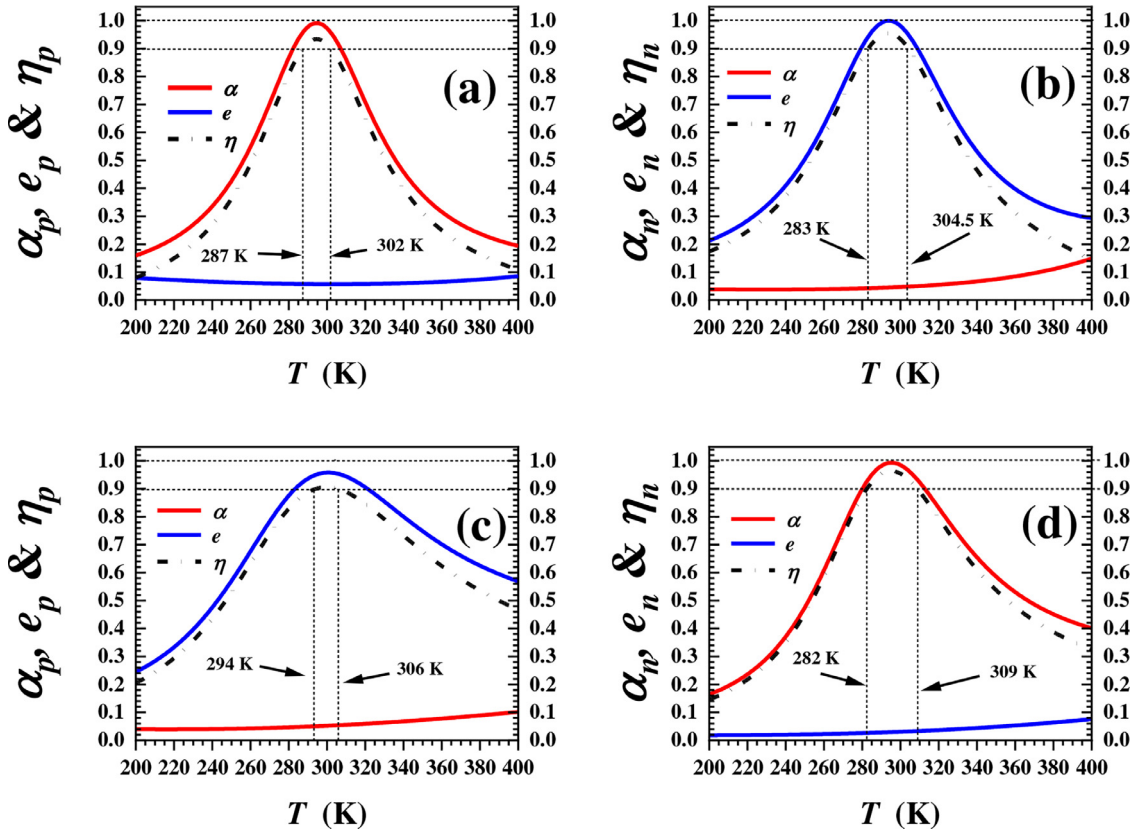

Fig. 7. The spectra of α_q, e_q and η_q relating to the temperature. (a) λ=4.692 μm for the FS, (b) λ=4.692 μm for the BS, (c) λ=3.890 μm for the FS, (d) λ=3.896 μm for the BS.

Associating Eqs. (20) and (21), it can be written as:

$$\alpha_q(-\theta) = e_q(\theta). \tag{22}$$

This is the general form of Kirchhoff's law [1]. Likewise, the form of $\alpha_q(\theta)$=e_q(-θ) is alright.

Besides, in this paper, the coefficient η_q=|$\alpha_q(\theta)$-$e_q(\theta)$| is borrowed here to describe the nonreciprocal properties.

3. Results and discussion

Assuming θ=45° and T = 300 K, Fig. 3 illustrates the spectra of α_q, e_q, and η_q for the FS and BS relating to the incident wavelength λ. For the FS in Fig. 3(a), the WDMSes displayed the properties of absorption and emission at 4.692 μm and 3.890 μm, respectively. Both of the peaks exceed 0.9 with the η_p values more than 0.9 at the same points as well in Fig. 3(b). Given in Fig. 3(d) for the BS, the structure exhibits nonreciprocal thermal radiation at similar frequency points. At λ=4.692 μm, η_n reaches 0.95, while the value of η_n is 0.959 at 3.896 μm. But the responses to EM waves are quite the opposite, that at 3.896 μm the absorption takes the lead and the emission dominates at 4.692 μm as shown in Fig. 3(c). Additionally, there is a peak of η_n reaching 0.953 at 4.832 μm and its absorption is far better than the emission. In comparison, the properties of the nonreciprocal thermal radiation for the BS are better than that for the FS, wherein the corresponding wave points, the η_n is no less than 0.95.

Figure 4 displays the normalized magnetic distribution in the WDMSes, which reveals the principle of absorption and emission based on the introduction of the defects. $|H_{in}|$ is the norm of the magnetic field of the incident EM waves in the free space. $|H_y|$ represents the norm of the magnetic fields related to the location in the structure. According to Eq. (22), high absorption at -θ indicates efficient emission at θ.

For the FS, Fig. 4(a) witnesses largely enhanced fields in the defect and L layers at θ=−45° and λ=3.890 μm. Subsequently, the envelope of the fields decays and gradually converges to zero through the structure. Here, the defect W layers and L layers can be viewed as a whole cavity. It is easy for the TM wave of λ=3.890 μm in the H layers to enter the cavity, while it is confronted with tremendous impedance as it tries to permeate from the cavity into the H layers. Great reflected waves on the interface coherent with the incident wave constructively interfere, in which case the energy is localized in the cavity in the form of the standing waves. Considering W is lossy, the cavity will consume the energy of the EM fields, which explains the absorption by the WDMSes at θ=−45°. In contrast, for the FS and θ=45° in Fig. 4(a), the strong fields are pooled at the incident port and suffer from fading exponentially which demonstrates most energies are reflected at the port rather than propagating through the layers. When it comes to absorption at θ=45° and λ=4.692 μm as given in Fig. 4(b), the pattern is similar to that at θ=−45° and λ=3.890 μm. What differs is that the fields of λ=4.692 μm at θ=45° are more effectively confined in the W layers. For the BS, equally, W and L layers working as a whole take on the function of localization. Under the circumstance of θ=45° and λ=3.896 μm, the standing wave in Fig. 4(c) vibrates at a higher amplitude in the L layer, verifying the effective absorption. Also, the field distribution of θ=−45°illustrates weak emission. Figure 4(d) denotes the distribution when λ is 4.692 μm. At θ=45°, energy is limited in the W medium and the absorption is strong, while the absorption at θ=−45° is feeble.

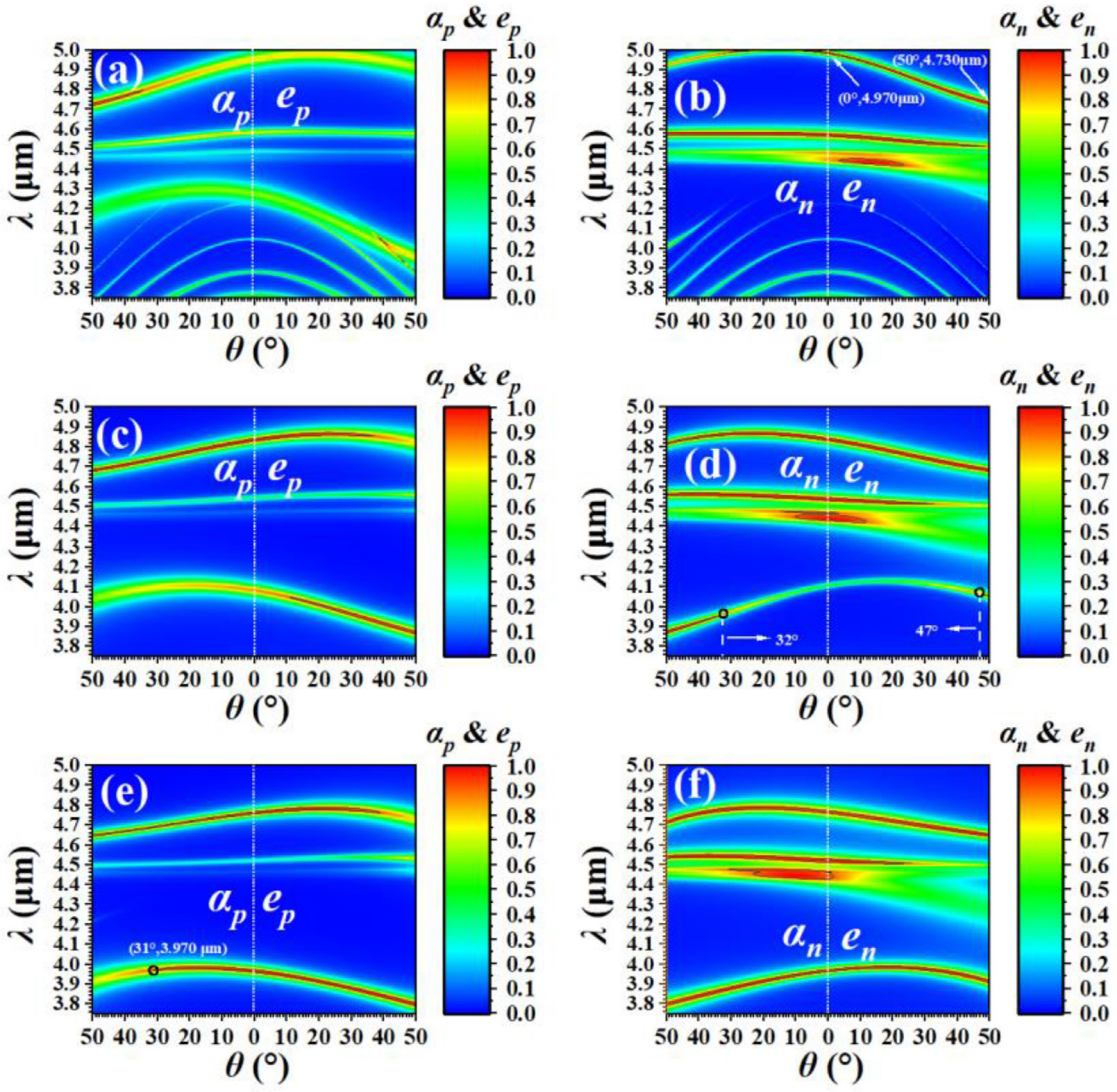

Fig. 8. Contour maps of α_q and e_q with different τs. (a) τ=0.2 for the FS, (b) τ=0.2 for the BS, (c) τ=0 for the FS, (d) τ=0 for the BS, (e) τ=−0.2 for the FS, (f) τ=−0.2 for the BS.

When T is 300 K, Fig. 5 exhibits the α_q, e_q, and η_q for the FS and BS under varying incident angle θ and wavelength λ. The solid black line outlines the regions where the values are greater than 0.9. As displayed in Fig. 5(a), along with the increasing θ, the α_p peak blueshifts from 4.832 μm to 4.680 μm. Over the same interval in the long wave band, the e_p peak moves reversely until θ=23° and then blueshifts to 4.850 μm at θ=36.5°. Moreover, there is an emission band originating at θ=10° whose center wavelength moves from 4.050 μm to 3.870 μm. For the BS in Fig. 5(c), over the band between 4.60 μm and 4.90 μm, rising θ transfers the emission peak to a shorter wave range, while the absorption peak turns to a long wave range and then blueshifts. Additionally, a wider θ brings about new emission and absorption bands at θ= 47° and 32° in the shorter wave range. The wave domains of the two share no overlap. The emission band is localized between 4.050 μm and 4.070 μm, as well as the absorption band from 3.870 μm to 3.960 μm.

Typically, the wider θ is, the more likely the nonreciprocity tends to exist. Figure 5(b) and (d) illustrate clearly that over the wider angular region, the absorption and emission peaks can be staggered to a better extent. With regards to the η_p for the FS in Fig. 5(b), the strong nonreciprocity can be realized at θ=15.5° and it proves distinct at θ= 31°∼33°, with three different wave ranges around 3.950 μm, 4.730 μm, and 4.860 μm. On the other hand, as to the η_n for the BS in Fig. 5(d), the strong nonreciprocity shows up at θ=15°. In the case of θ more than 35°, there exist three significantly nonreciprocal wave bands as well.

Figure 6 reveals the evolutions of T on the WDMSes properties at θ= 45°. As given in Figs.6(a) and (c), a higher T motivates the bands of both the absorption and emission towards the long wave range. In Fig. 6(a), the absorption band covers a wider temperature range from 200 K to 371 K in the interval between 4.648 μm and 4.732 μm, and there is an additional absorption band at 371 K around λ=4.084 μm. As to the emission region, the relevant band originates at T = 272 K. In the long wave band in Fig. 6(c), over the similarly corresponding range between 4.648 μm and 4.752 μm, the emission band ranges from 200 K to 400 K. High T eliminates the absorption band over T = 378 K.

When it comes to the FS, in Fig. 6(b), in the temperature region between 295 K and 328 K, the η_p is more than 0.9 around the two wavebands at 3.890 and 4.700 μm approximately. Also, a high T gives rise to the nonreciprocal band at T more than 361 K in the

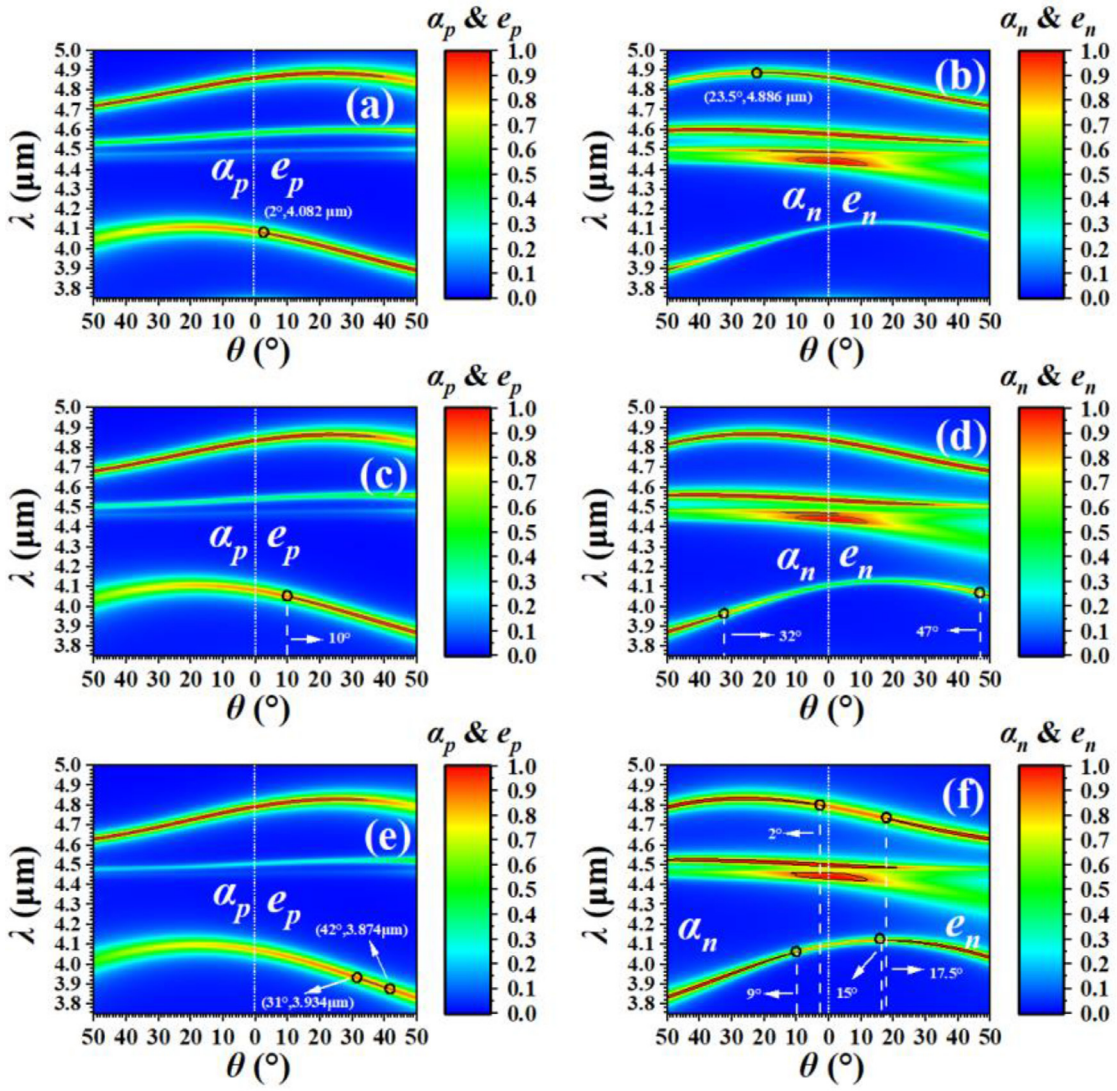

Fig. 9. Diagrams of α_q and e_q with varying defect thicknesses. (a) d_W=1.2 μm for the FS, (b) d_W=1.2 μm for the BS, (c) d_W=1 μm for the FS, (d) d_W=1 μm for the BS, (e) d_W=0.8 μm for the FS, (f) d_W=0.8 μm for the BS.

long wave range. In terms of the BS, Fig. 6(d) puts it that the nonreciprocity arises in the low T and completely disappears at 366 K. It is worth noticing that in the interval between 4.040 μm and 4.060 μm, there is a narrow band in the width about 0.006 μm.

As θ is taken as 45°, Fig. 7 displays α_q, e_q, and η_q at various T for the FS and BS. The η_q spectra put a bell-shaped distribution with temperature. For the FS in Fig. 7(a), η_p is more than 0.9 in the range from T = 287 K to T = 302 K at 4.692 μm. Given in Fig. 7(c) at 3.890 μm, the WDMSes have the properties of strong nonreciprocal thermal radiation from T = 294 K to T = 306 K. For the BS, the nonreciprocity is relatively stable over a wider temperature range. At 4.692 μm in Fig. 7(b), η_n exceeds 0.9 between T = 283 K and T = 304.5 K. Similarly, at 3.896 μm, η_n maintains more than 0.9 from T = 282 K to T = 309 K, as illustrated in Fig. 7(d).

The thickness of the unit U can be written as:

$$d_{unit} = (1 + \tau) \cdot (d_H + d_L) \tag{17}$$

Under T = 300 K, the coefficient τ is modified to test the effects of optical length on the nonreciprocity. Compared to the radiation properties with τ=0 in Fig. 8(c), a longer optical length with τ=0.2 weakens the absorption and emission for the FS in Fig. 8(a). As shown, there is an emission band over the long wave range attaining 36.5° in the angular range in Fig. 8(c) and the absorption band is from 0° to 50°. Yet, in Fig. 8(a), the emission band disappears and the absorption band originates at θ=39.5°. The phenomenon in Fig. 8(e) demonstrates τ=−0.2 does significant effects on the bands in the short wavelength range. The shortened optical length results in the absorption in the angular range from 0° to 31° and the emission from 0° to 50°. Given in Fig. 8(b), for the BS, τ=0.2 drives the relevant bands to a longer wave region and the emission band gets more sensitive to the changing θs, that its peak moves from 4.970 μm to 4.730 μm together with rising θ. Besides, the absorption band is localized to 4.970 μm or more. In the angular range from 2.5° to 34.5°, the absorption and emission wave domains do not intersect at all.

In Fig. 8(d), the absorption and emission bands originate at θ=32° and 47°, respectively. Also, given in Fig. 8(f), the absorption and emission are visibly enhanced covering the angular region from 0° to 50° in the short wavelength range. Generally speaking, the changing optical length of the unit affects the Bragg scattering conditions, in which case, the longer optical length induced the shift of the wavebands towards the long wave domain, and

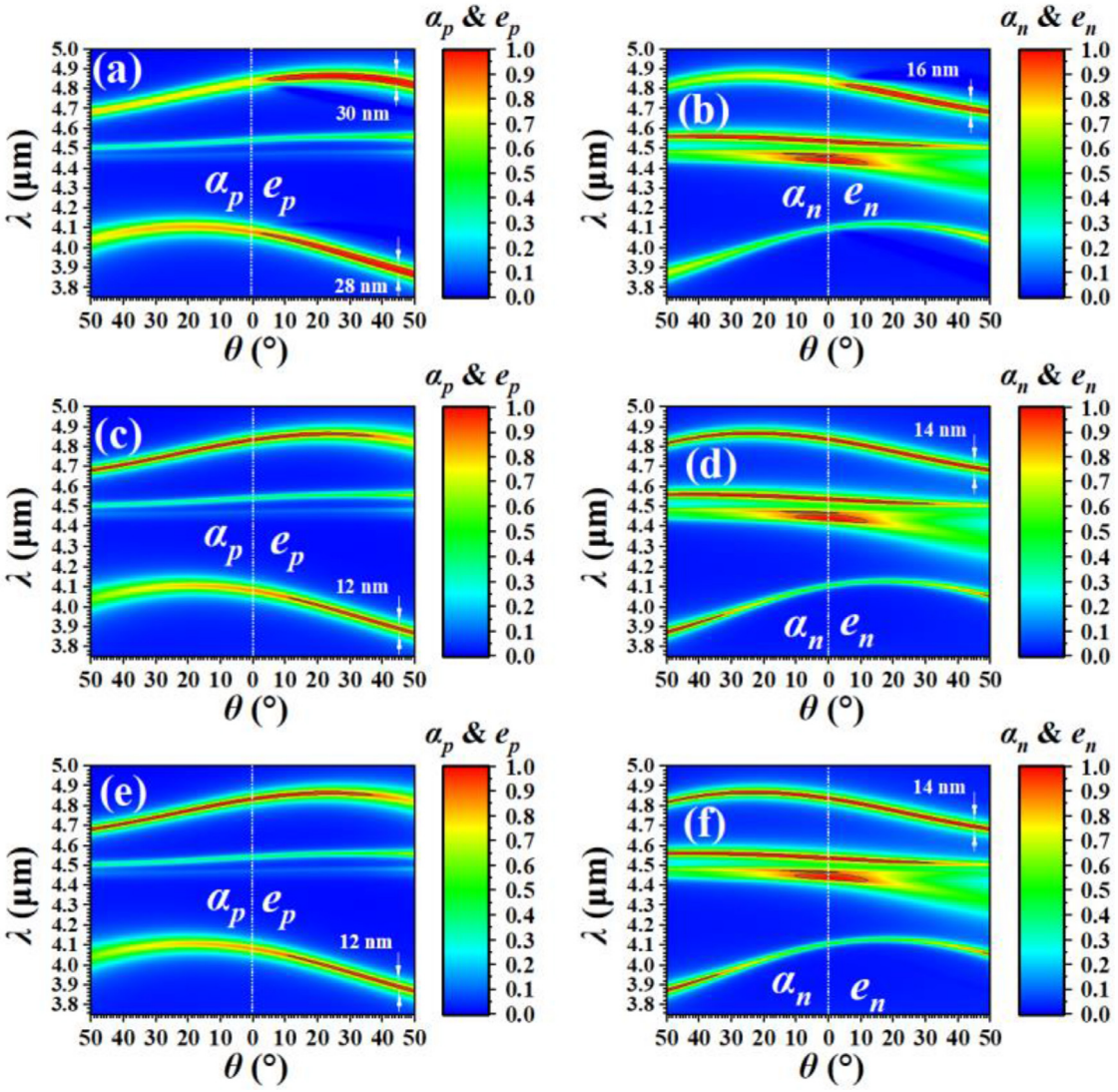

Fig. 10. The contour maps of α_q and e_q with varying N. (a) $N = 2$ for the FS, (b) $N = 2$ for the BS, (c) $N = 4$ for the FS, (d) $N = 4$ for the BS, (e) $N = 8$ for the FS, (f) $N = 8$ for the BS.

the wave bands prefer to blueshift on behalf of the short optical length.

Figure 9 exhibits the influences of the defect thicknesses on the thermal properties. Deviation of the defect thicknesses fails to shift the absorption or emission bands in the study wave region. For the FS, the thickness has particular effects over the short wavelength band where the angular range of the emission is wider in the case of thicker W layers. When d_W is set as 1.2 μm in Fig. 9(a), the emission spectrum extends from 2° to 50°. In comparison to the emission band in Fig. 9(c), the angular range covers a span from 10° to 50°. When it comes to d_W=0.8 μm in Fig. 9(e), the corresponding band is restricted between 31° and 42°. For the BS, thicker defects impair the absorption in the wider angular scope. The absorption of the EM waves originates at θ=0° and ends up at θ=23.5° in Fig. 9(b). However, the two bands both cover the angular span from θ=0° to 50° in Fig. 9(d). As shown in Fig. 9(f), over the long wave range, the absorption and emission bands shrink in the angular range and they originate at θ=2° and 17.5°, respectively. Slimmer defects contribute to widening the angular range in the short wavelength region as well. In Fig. 9(f), the absorption band extends to 9° and the emission band reaches 15° significantly. According to the analysis of the principle demonstrated in Fig. 4, the thickness of the defects determines the optical length of the resonant cavity, and changing optical lengths makes a difference to the localization capability, as a result of which the absorption and emission bands cover various regions.

Given T = 300 K, Fig. 10 illustrates the thermal properties with different N. In the case of $N = 2$, the absorption bands disappear in the long wave range for both the FS and BS, while the emission band is generally extended in the angle and wave range. Taken as an example, for the wave of θ=45° in Fig. 10(a), the emission band covers the span of 28 nm from 3.876 μm to 3.904 μm and the span of 30 nm from 4.818 μm to 4.848 μm, respectively. Also, in the case of θ=45° and for BS in Fig. 10(b), the emission band is located between 4.688 μm and 4.704 μm about 16 nm in width. In comparison, rising N narrows the emission band down. The emission bandwidths of $N = 4$ and 8 are the same. In Fig. 10(c) and (e) for the FS, at θ=45°, the emission wave bands are 12 nm in width from 3.886 μm to 3.898 μm. Besides, for the BS in Fig. 10(d) and (f), the emission bands range from 4.688 μm to 4.702 μm about

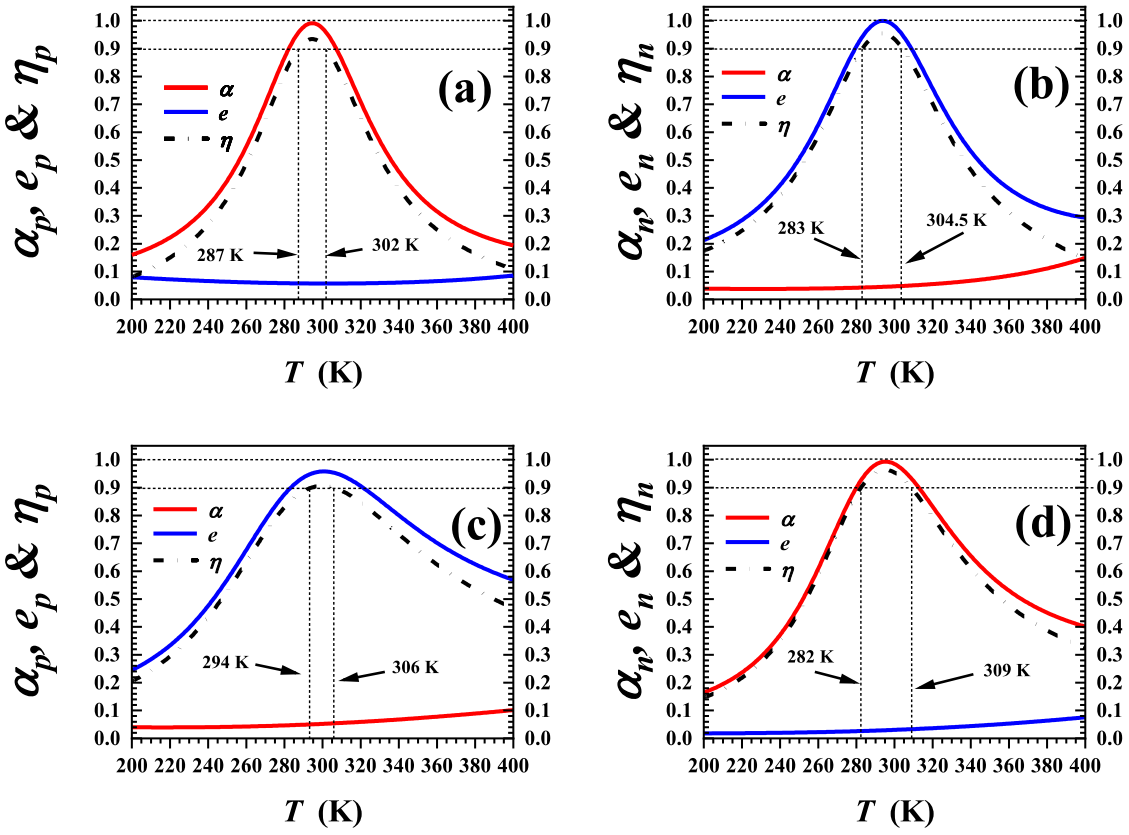

Fig. 11. The spectra of α_q, e_q, and η_q around 4.692 μm with $N = 8$. (a) α_p and e_p for the FS, (b) η_p for the FS, (c) α_n and e_n for the BS, and (d) η_n for the BS.

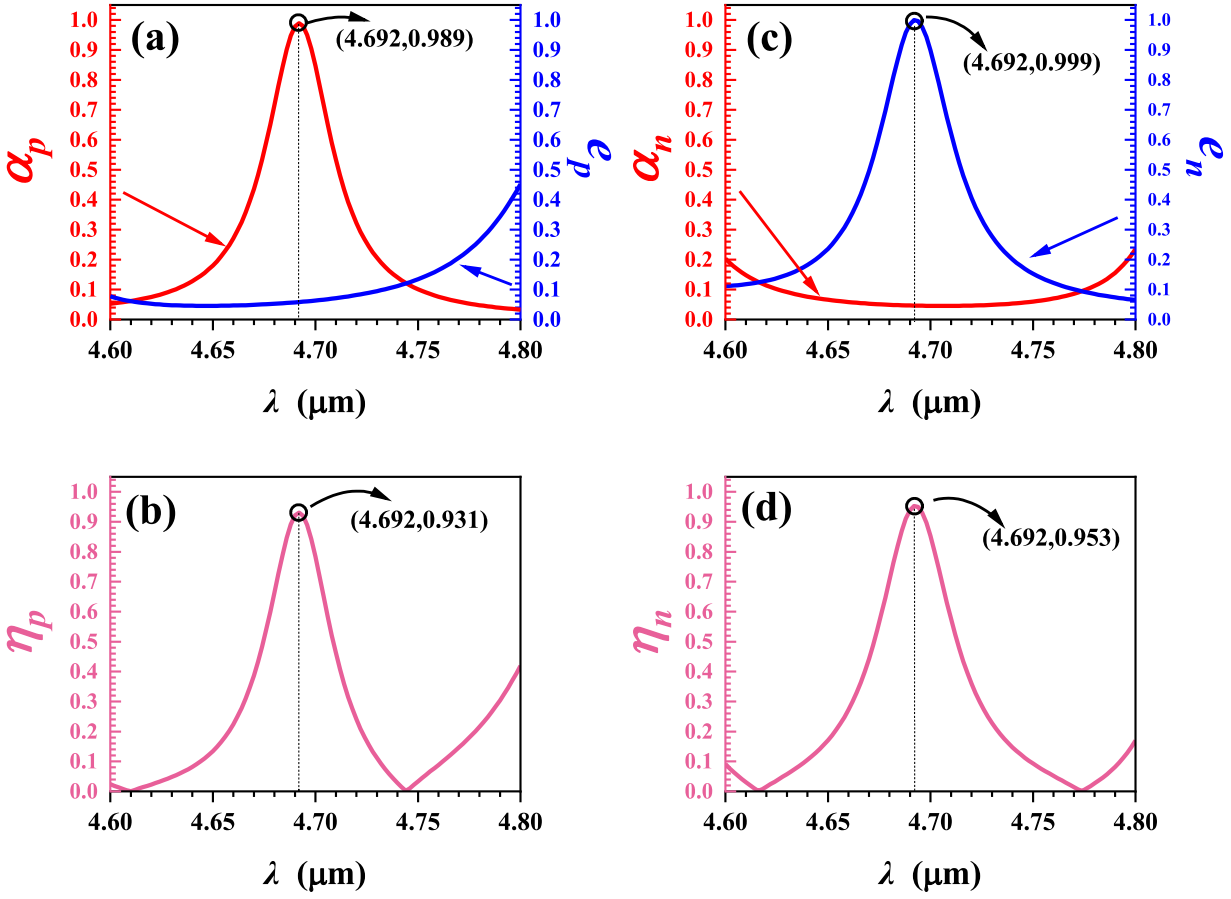

Fig. 12. The spectra of α_q, e_q, and η_q around 4.692 μm with $N = 4$. (a) α_p and e_p for the FS, (b) η_p for the FS, (c) α_n and e_n for the BS, and (d) η_n for the BS.

14 nm in width. The thermal radiation properties of $N = 4$ and 8 are similar in that the wave band and angular range lie in the same domains.

For the stacked dielectric layer $(HL)^N$ with the period N, generally speaking, larger N will account for the surface of the stacked layers reflecting the EM waves over a wider wavelength and angular range. However, the effects of N may approach saturation that in case N steps up to some degree, the capacity of the stacked layers reflecting the EM waves with certain wavelengths and angles of incident tends to be constant. Here in Fig. 10, when N increases from 2 to 4, the absorption and emission bands experience visible changes. Because the larger N blocks the EM waves, in the wider wavelength and angular ranges, coupling into $(HL)^N$, then the EM waves are confined in the cavity and wear out. However, the continued increase of N to 8 has limited impacts on $(HL)^N$. Therefore, the absorption and emission bands at $N = 8$ are similar to those at $N = 4$. Despite the weak effects, yet, it is capable of optimizing the peaks of α_q, e_q, and η_q on a small scale.

Figure 11 shows the spectrum of α_q, e_q, and η_q around 4.692 μm. For the FS in Fig. 11(a), the absorption takes the lead at 4.692 μm, reaching 0.989. In correspondence, the peak of η_p in Fig. 11(b) is localized at 4.692 μm. Figure 11(c) illustrates the emission peak for the BS at 4.692 μm. Rather, the η_n in Fig. 11(d) attains its maximum at 4.692 μm. Obviously, $N = 8$ brings about the peaks of α_q, e_q, and η_q lying in the same wave point exactly.

Comparatively, when it comes to $N = 4$ in Fig. 12, the wave points of the extremes are staggered a little, where the peaks of η_q for the FS and BS are 4 nm apart in Fig. 12(b) and (d). They stand at 4.692 μm and 4.696 μm, respectively. Besides, the absorption peak for the FS as well as the emission peak for the BS lies at different points equally. In Fig. 12(a), the absorptivity for the FS is 0.983 at λ=4.694 μm at its maximum, while the emission peak for the BS is 0.999 at λ=4.692 μm, given in Fig. 12(c). To be concluded, though too much N makes little difference to the thermal radiation property, it is an available method to adjust the peak shifting on a small scale.

4. Conclusion

To be concluded, this work proposes the WDMSes to realize the nonreciprocal thermal radiation on both sides operating over the mid-infrared wave range. A generalized Kirchhoff's law is derived in the paper. Assuming the object is opaque and the wavelength of the EM wave is fixed, it can be written as $\alpha_q(\theta)=e_q(-\theta)$ or $\alpha_q(-\theta)=e_q(\theta)$. In this structure, the defect layers are capable of localizing fields around the defect, thus yielding absorption. In terms of $T = 300$ K and $\theta=45°$, for the FS, the absorption is stronger than the emission at 4.692 μm, while at 3.890 μm the emission proves more efficient. For the BS, the WDMSes function as an effective emitter at 4.692 μm. But the emission is far weaker than the absorption at 3.896 μm. Comparably, the nonreciprocity of the BS is stronger than that of the FS. η_q reaches 0.95 at 4.692 μm and 3.896 μm for the BS, while it merely exceeds 0.9 at 4.692 μm and 3.89 μm for the FS. Besides, for the BS, the structure can maintain strong nonreciprocal properties over a wider temperature range than that for the FS. The η_q spectra for the BS cover a span of 30 K at 4.692 μm and 20 K at 3.896 μm with η_q more than 0.9. θ makes a difference to the nonreciprocity. The wider the incident angle θ, the better the absorption and emission bands tend to be staggered over the wave band. For both the FS and BS, the strong nonreciprocity originates around $\theta=15°$. What's more, the thicknesses of the dielectric layer unit d_w and the period N are adjusted to investigate the effects. In general, the thicker unit is inclined to shift the whole band toward the long wave range while the case of the slimmer unit is on the contrary. In addition, increasing N narrows the absorption or emission band in the wave range and broadens the angular range. Too much N makes sense in modifying the spectrum peaks on the small scale. The work provides an idea for the design of efficient heat radiation transfer media, energy conversion devices, and so on. And many works remain to be done about extending the working bandwidth, angular range, and so on.

Declaration of Competing Interest

None

CRediT authorship contribution statement

You-Ming Liu: Data curation, Formal analysis, Writing – original draft. **Yuan-Kun Shi:** Investigation, Software. **Dan Zhang:** Visualization, Funding acquisition. **Hai-Feng Zhang:** Conceptualization, Writing – review & editing.

Data availability

Data will be made available on request.

Acknowledgement

This work was supported by the College Student Innovation Training Program of Nanjing University of Posts and Telecommunications, and the Jiangsu Agriculture Science and Technology Innovation Fund (JASTIF) (Grant No.CX(21)3187).

Appendix A. Transfer matrix method

In this work, the TMM is utilized to numerally simulate all the spectrums of the thermal properties. TMM takes the multiple reflections and transmissions at interfaces into consideration and builds up the bridge of the EM fields between the layers. The calculated results are the analytical solutions. The detailed derivation is available in Ref.33 and Ref.35. Besides, the finite element analysis (FEA) is a conventional way to solve Maxwell's equations as well. By analyzing the elements of the structure, it can induce the S-parameters. To ensure the accuracy of the TMM, the commercial software HFSS, of which the algorithm is based on the FEA, is put in use to compare the results calculated by the two methods in the following Fig. A1.

The absorption spectra are obtained in the case of $\theta=0°$ and $T = 300$ K. Obviously, under the same conditions, the spectra have similar trends. Yet, as to the specific values, they differ. In Figs.A1(a) and (b), the distinct absorption peaks are located at the incident wavelength λ=4.834 μm and 4.832 μm. They are 0.02 nm apart. Additionally, the absorptivity at the peak calculated by the TMM is higher, of which it is 0.935. In the same way, when it comes to the BS in Fig. A1(c), there are three peaks at λ=4.437 μm, 4.536 μm, and 4.837 μm. The absorption peaks in Fig. A1(d) also fall at similar wavelengths, the variance of which is no more than 3 nm. Normally, the absorptivity in Fig. A1(d) is higher than that in Fig. A1(c) as well. The peaks are all 0.998 in Fig. A1(d), while in Fig. A1(c) the higher absorptivity is only 0.952.

The absorptivity calculated by the TMM and FEA is a little different. On one hand, the results based on the FEA are approximate solutions that are close to the true results. More discrete meshing will bring about more accurate results. On the other hand, the TMM fails to take into account the influences on the EM fields at the interfaces between the two layers. In general, they are weak. However, in some cases when the influences brought by the interfaces dominate, they cannot be neglected as well.

Generally speaking, although for the model in this paper, there are some differences in the calculated results by the TMM and the

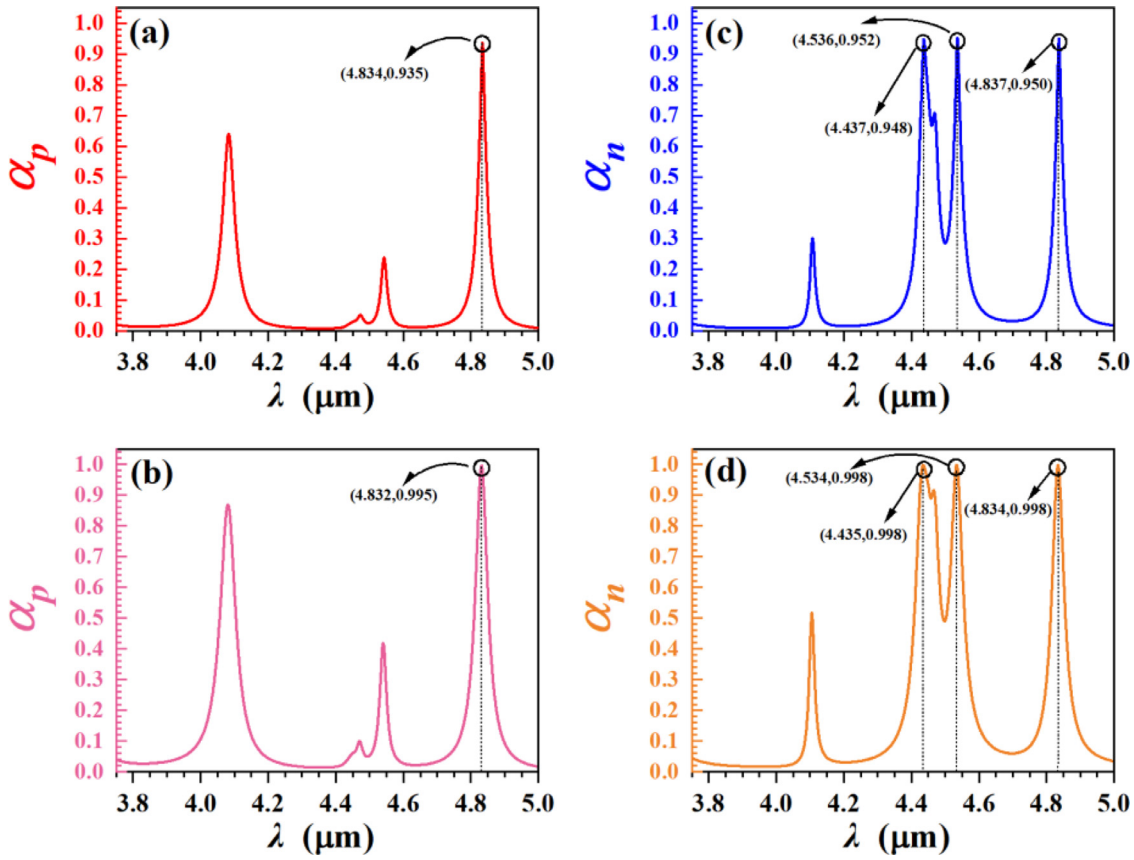

Fig. A1. The comparison between the two calculated methods. (a) the FEA for the FS, (b) the TMM for the FS, (c) the FEA for the BS, (d) the TMM for the BS.

FEA, and they can be ignored, in terms of the approximate values of the absorptivity and similar wavelengths corresponding to the extreme point. Also, the spectra share the same trend related to the wavelength. Therefore, the data obtained in this paper based on TMM are plausible.

Appendix B. Nonreciprocal thermal radiation

The formula of absorptivity and emissivity are derived in detail here. There are three bodies at the same temperature T in the free space, given in Fig. B1. Two black bodies BL_1 and BL_2 are lain on both sides of the heat source S and have far-field effects on it.

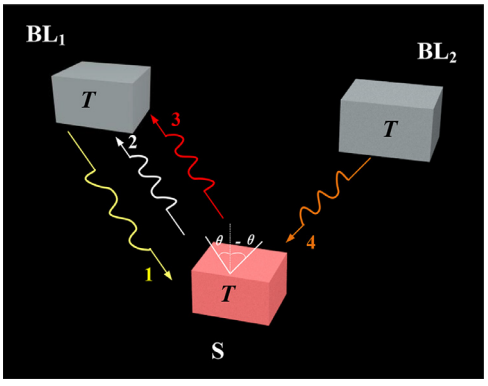

Fig. B1. The three body system concerning a heat source and two blackbodies at the same temperature T. Four key processes are marked: process 1 (yellow line): emission from BL_1 to S, process 2 (white line): emission from BL_1 to S, process 3 (red line): reflected EM radiation from BL_2 to BL_1 and process 4 (orange line): emission from BL_2 to S.

Considering the radiated EM waves from the BL_1 incident on the surface of S at θ, the waves from the BL_2 are at $-\theta$.

The thermal exchange between BL_1 and S is put on the focus and four related key processes are marked in Fig. B1. Supposing negligible energy transmitted through S, one can attain:

$$R(\theta) + \alpha(\theta) = 1, \tag{B1}$$

where $R(\theta)$ indicates the reflectivity of the EM waves from BL_1 and $\alpha(\theta)$ measures how much energy from the same direction is absorbed. For another, the energy flowing in the direction from S to BL_1 consists of two components: the emission from S to BL_1 and the reflected emission from blackbody BL_2. The EM waves from BL_2 transmitted through the surface are also considered to approach zero. Provided the second law of thermodynamics, no net energy flow in and out of the blackbody BL_1. It can be deduced:

$$R(-\theta) + e(\theta) = 1. \tag{B2}$$

The final derivation absorptivity $\alpha(\theta)$ and emissivity $e(\theta)$ are as follows:

$$\alpha(\theta) = 1 - R(\theta), \tag{B3}$$

$$e(\theta) = 1 - R(-\theta). \tag{B4}$$

For general materials, $R(\theta)$ and $R(-\theta)$ are equal, in which case $\alpha(\theta)$ and $e(\theta)$ are numerically the same, and conform to the conventional Kirchhoff's law. Yet, the nonreciprocal material results in $R(\theta) \neq R(-\theta)$, thus bringing about $\alpha(\theta) \neq e(\theta)$. As a result, the more generalized Kirchhoff's law should be expressed as $\alpha(\theta) = e(-\theta)$ on the condition of the same incident wavelength. Although the conventional Kirchhoff's law is broken, yet, it should be put on the emphasis that BL_1, BL_2, and S still follow the second law of thermodynamics exactly. And Eqs. (B3) and (B4) have no conflict with the law throughout the whole derivation.

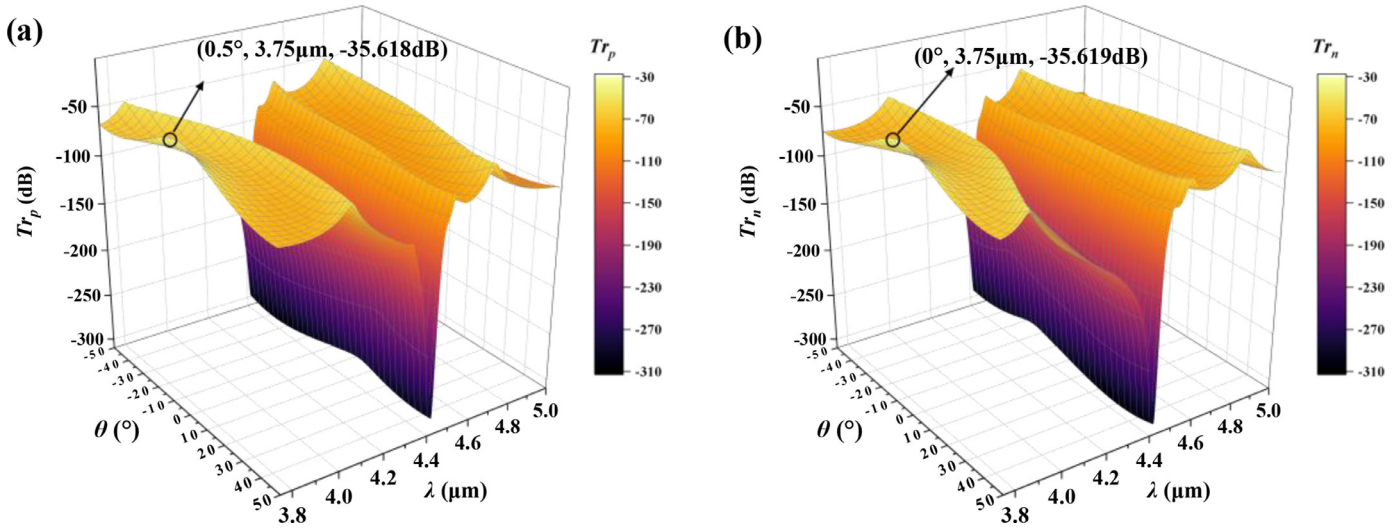

Fig. B2. the related transmissivity of EM waves propagating at the incident angle θ ranging from $-50°$ to $50°$ for the FS and BS. (a) Transmissivity of EM waves propagating for the FS. (b) Transmissivity of EM waves propagating for the BS.

As denoted, the formula of absorptivity α and emissivity e in Eqs. (B3) and (B4) can only be applied to the condition where the transmissivity of the EM waves through one object is relatively low regardless of the incident angle. In our work, the designed WDMSes fit well. Fig. B2 displayed the relevant transmissivity of EM waves propagating at the incident angle θ ranging from $-50°$ to $50°$ for the FS and BS, respectively.

For the FS in Fig. B2(a), when the EM waves with wavelength 3.75 μm incident at θ=0.5°, the transmissivity reaches its maximum −35.618 dB In the same way, the higher transmissivity for the BS in Fig. B2(b) is merely −35.619 dB in the case of θ=0 .

References

[1] Remer L, Mohler E, Grill W, Lüthi BJPRB. Nonreciprocity in the optical reflection of magnetoplasmas. Phys Rev B 1984;30(6):3277.
[2] Zhang ZM, Wu X, Fu C. Validity of Kirchhoff's law for semitransparent films made of anisotropic materials. J Quant Spectrosc Radiat Transf 2020;245:106904.
[3] Park Y, Zhao B, Fan S. Reaching the ultimate efficiency of solar energy harvesting with a nonreciprocal multijunction solar cell. Nano Lett. 2021;22(1):448–52.
[4] Pajovic S, Tsurimaki Y, Qian X, Boriskina SV. Radiative heat and momentum transfer from materials with broken symmetries: opinion. Opt Mater Express 2021;11(9):3125–31.
[5] Bi L, Hu J, Jiang P, Kim HS, Kim DH, Onbasli MC, Dionne GF, Ross CA. Magneto-optical thin films for on-chip monolithic integration of non-reciprocal photonic devices. Materials 2013;6(11):5094–117.
[6] Li WK, Guo GY. First-principles study on magneto-optical effects in the ferromagnetic semiconductors $Y_3Fe_5O_{12}$ and $Bi_3Fe_5O_{12}$. Phys Rev B 2021;103(1):014439.
[7] Zhu L, Fan S. Near-complete violation of detailed balance in thermal radiation. Phys Rev B 2014;90(22):220301.
[8] Zhao B, Shi Y, Wang J, Zhao Z, Zhao N, Fan S. Near-complete violation of Kirchhoff's law of thermal radiation with a 0.3 T magnetic field. Opt Lett 2019;44(17):4203–6.
[9] Wu J, Wu B, Wang Z, Wu X. Strong nonreciprocal thermal radiation in Weyl semimetal-dielectric multilayer structure. International Journal of Thermal Sciences 2022;181:107788.
[10] Wu J, Wang Z, Zhai H, Shi Z, Wu X, Wu F. Near-complete violation of Kirchhoff's law of thermal radiation in ultrathin magnetic Weyl semimetal films. Opt Mater Express 2021;11(12):4058–66.
[11] Li T, Yin C, Wu F. Strong optical non-reciprocity in one-dimensional photonic crystal containing a Weyl semimetal-based defect. Opt Mater 2021;121:111583.
[12] Wu X, Yu H, Wu F, Wu B. Enhanced nonreciprocal radiation in Weyl semimetals by attenuated total reflection. AIP Adv 2021;11(7):075106.
[13] Zhao B, Guo C, Garcia CA, Narang P, Fan S. Axion-field-enabled nonreciprocal thermal radiation in Weyl semimetals. Nano Lett. 2020;20(3):1923–7.
[14] Liu R, Ge L, Wu B, Cui Z, Wu X. Near-field radiative heat transfer between topological insulators via surface plasmon polaritons. Iscience 2021;24(12):103408.
[15] Park Y, Asadchy VS, Zhao B, Guo C, Wang J, Fan S. Violating Kirchhoff's law of thermal radiation in semitransparent structures. ACS Photonics 2021;8(8):2417–24.
[16] Wu J, Wu F, Wu X. Strong dual-band nonreciprocal radiation based on a four–part periodic metal grating. Opt Mater 2021;120:111476 .
[17] Wu X, Liu R, Yu H, Wu B. Strong nonreciprocal radiation in magnetophotonic crystals. J Quant Spectrosc Radiat Transf 2021;272:107794.
[18] J. Wu, F. Wu, T. Zhao, H. Zhai and X. Wu, "Nonreciprocal thermal radiation based on Fibonacci quasi-periodic structures," arXiv preprint arXiv:2109.05134(2021)
[19] Xue C, Jiang H, Chen H. Highly efficient all-optical diode action based on light–tunneling heterostructures. Opt Express 2010;18(7):7479–87.
[20] Hu X, Li Z, Zhang J, Yang H, Gong Q, Zhang X. Low-power and high-contrast nanoscale all-optical diodes via nanocomposite photonic crystal microcavities. Adv Funct Mater 2011;21(10):1803–9.
[21] Gevorgyan AH, Golik SS, Gevorgyan TA. Diode based on magneto-photonic crystals. J Magn Magn Mater 2019;474:173–82.
[22] Chetvertukhin AV, Sharipova MI, Zhdanov AG, Shapaeva TB, Dolgova TV, Fedyanin AA. Femtosecond time-resolved Faraday rotation in thin magnetic films and magnetophotonic crystals. J Appl Phys 2012;111(7):07A944.
[23] Goto T, Baryshev AV, Tobinaga K, Inoue M. Faraday rotation of a magnetophotonic crystal with the dual-cavity structure. J Appl Phys 2010;107(9):09A946.
[24] Ma H, Ju C, Xi X, Wu RX. Nonreciprocal Goos-Hänchen shift by topological edge states of a magnetic photonic crystal. Opt Express 2020;28(14):19916–25.
[25] Mao M, Zhang T, Guo S, Zhang H. Goos–Hänchen shift produced by a one-dimensional photonic crystal doped with InSb. JOSA B 2020;37(7):2095–103.
[26] Singh BK, Pandey PC. Effect of temperature on terahertz photonic and omnidirectional band gaps in one-dimensional quasi-periodic photonic crystals composed of semiconductor InSb. Appl Opt 2016;55(21):5684–92.
[27] Pandey JP. Omnidirectional high reflectors using 1-D photonic crystals. Int J Phys Sci 2017;12(12):137–45.
[28] Abdulhalim I. Reflective phase-only modulation using one-dimensional photonic crystals. J Opt A Pure Appl Opt 2000;2(2):L9–L11.
[29] Li Z, Palacios E, Butun S, Kocer H, Aydin K. Omnidirectional, broadband light absorption using large-area, ultrathin lossy metallic film coatings. Sci Rep 2015;5(1):1–8.
[30] Li H, Qin M, Wang L, Zhai X, Ren R, Hu J. Total absorption of light in monolayer transition-metal dichalcogenides by critical coupling. Opt Express 2017;25(25):31612–21.
[31] Bian LA, Deng Z, Hong Y, Qiu Y, Liu Z, Xiao P, Li G. Double-mode absorption in double-defect photonic crystal with one graphene multilayer. Optical and Quantum Electronics 2020;52(3):1–10.
[32] Wu F, Wu X, Xiao S, Liu G, Li H. Broadband wide-angle multilayer absorber based on a broadband omnidirectional optical Tamm state. Opt Express 2021;29(15):23976–87.
[33] Qi L, Yang Z, Lan F, Gao X, Shi Z. Properties of obliquely incident electromagnetic wave in one-dimensional magnetized plasma photonic crystals. Phys Plasmas 2010;17:042501.
[34] Asadchy VS, Guo C, Zhao B, Fan S. Sub-wavelength passive optical isolators using photonic structures based on Weyl semimetals. Adv Opt Mater 2020;8(16):2000100.
[35] Wu X. The promising structure to verify the Kirchhoff's law for nonreciprocal materials. ES Energy Environ 2021;12(3):46–51.
[36] Wang H, Li YP. An eigen matrix method for obtaining the band structure of photonic crystals. Acta Physica Sinica 2001;50(11):2172–8.